RSC Advances

PAPER

View Article Online
View Journal | View Issue

Cite this: *RSC Adv.*, 2024, **14**, 28244

High photocatalytic efficiency of a ZnO nanoplate/Fe_2O_3 nanospindle hybrid using visible light for methylene blue degradation

Nguyen Dac Dien,[a] Thi Thu Ha Pham,[b] Xuan Hoa Vu, *[c] Vuong Truong Xuan, [b] Thi Thu Thuy Nguyen,[b] Tran Thu Trang,[c] Nguyen Van Hao, [c] Pham Thi Nga,[cd] Tran Thi Kim Chi,[e] Tran Thi Huong Giang[e] and Nguyen Duc Toan[f]

In this work, ZnO nanoplates and Fe_2O_3 nanospindles were successfully fabricated *via* a simple hydrothermal method using inorganic salts as precursors. The ZnO/Fe_2O_3 hybrid was fabricated using a mechanical mixture of two different ZnO : Fe_2O_3 weight ratios to investigate the effect of weight ratio on catalytic properties. Scanning electron microscopy (SEM) and transmission electron microscopy (TEM) images showed that ZnO nanoplates (NPls) are about 20 nm thick with lateral dimensions of 100 × 200 nm, and Fe_2O_3 nanospindles (NSs) are about 500 nm long and 50 nm wide. X-ray diffraction (XRD) patterns revealed the successful formation of the ZnO, Fe_2O_3, and ZnO/Fe_2O_3 samples and indicated that their crystallite sizes varied from 20 to 29 nm depending on the ZnO : Fe_2O_3 weight ratio. Ultraviolet-visible (UV-vis) spectra showed that the bandgap energies of ZnO and Fe_2O_3 were 3.15 eV and 2.1 eV, respectively. Energy dispersive X-ray spectroscopy (EDS) results revealed the successful combination of ZnO and Fe_2O_3. Photocatalytic activity of the materials was evaluated through the degradation of methylene blue (MB) in aqueous solution under green light-emitting diode (GLED) irradiation. The results indicated that the ZnO/Fe_2O_3 composite showed a remarkable enhanced degradation capacity compared to bare ZnO NPls and Fe_2O_3 NSs. The ZnO : Fe_2O_3 = 3 : 2 sample demonstrated the best performance among all samples under identical conditions with a degradation efficiency of 99.3% for MB after 85 min. The optimum photocatalytic activity of the sample with ZnO : Fe_2O_3 = 3 : 2 was nearly 3.6% higher than that of the pure ZnO sample and 1.12 times more than that of the pristine Fe_2O_3 sample. Moreover, the highest photo-degradation was obtained at a photocatalyst dosage of 0.25 g l^{-1} in dye solution.

Received 10th June 2024
Accepted 14th August 2024

DOI: 10.1039/d4ra04230a

rsc.li/rsc-advances

1. Introduction

As industrial activities persistently expand, the necessity to eliminate or convert toxic contaminants present in wastewater into non-hazardous substances has become progressively critical.[1] Methylene blue (MB) is broadly used in the textile industry and is well known for its high toxicity to humans and the ecosystem. Apparel is a fundamental requirement within society; however, the environmental repercussions of textile effluents are significant and cannot be overlooked. Wastewater generated in large volumes from industrial activities poses a great challenge in developing countries such as Vietnam. MB can cause many adverse effects, including vomiting, diarrhoea, nausea, and burning eyes.[2] Scientific studies have elucidated practical approaches for the elimination or degradation of MB from these effluent sources to protect water bodies and living creatures. Several conventional methods adopted by textile factories for the treatment of MB, such as adsorption, membrane filtration, and reverse osmosis, do not thoroughly eradicate the pollutant but only transport it from one medium to another; therefore, the remaining absorbed persistent harmful chemicals result in secondary pollution, affecting the environment.[3] The potential for adsorbent reusability is impeded by active site saturation, while the degradation of pollutants through biodegradation pathways entails protracted temporal scales.[4] Therefore, it is necessary to develop a more effective process for removing MB from the environment.

[a]*Faculty of Occupational Safety and Health, Vietnam Trade Union University, 169 Tay Son Street, Dong Da District, Hanoi City, Vietnam*

[b]*Faculty of Chemistry, TNU-University of Sciences, Tan Thinh Ward, Thai Nguyen City, Vietnam*

[c]*Institute of Science and Technology, TNU-University of Sciences, Tan Thinh Ward, Thai Nguyen City, Vietnam. E-mail: hoavx@tnus.edu.vn*

[d]*Faculty of Secondary School, Hoa Lu University, 2 Xuan Thanh Street, Ninh Nhat Commune, Ninh Binh City, Vietnam*

[e]*Institute of Materials Science, Vietnam Academy of Science and Technology, 18 Hoang Quoc Viet Road, Cau Giay District, Ha Noi City, Vietnam*

[f]*Centre for Quantum Electronics, Institute of Physics, Vietnam Academy of Science and Technology, 10 Dao Tan, Ba Dinh District, Ha Noi City, Vietnam*

Photocatalytic oxidation using semiconductor oxides has been widely used because of its potential to completely degrade persistent pollutants. The application of both pure and modified semiconductor photocatalysts for water purification has undergone extensive investigation concerning the elimination of organic pollutants.[5] Wastewater issues can be addressed through the application of low-cost and environment-friendly semiconductor metal oxide materials, which have been proven effective in the removal of hazardous organic compounds without piling up toxic sludge.[6,7] Semiconductor photocatalysts absorb photons with energy higher than their bandgaps to excite electrons from the valence band to the conduction band and create holes in the valence band. Such electrons and holes are called photoexcited (photogenerated/photoinduced) charge carriers.[8] Photo-induced charge carriers actively engage in redox processes, leading to the formation of highly reactive species, including hydroxyl ($^{\bullet}OH$) and superoxide anion ($^{\bullet}O_2^-$) radicals from dissolved oxygen or water. These species will degrade the organic molecules present in the water to CO_2 and H_2O.[9,10] The specific pollutants and their properties within wastewater dictate the selection of suitable photocatalysts, operating conditions, and reactor designs for achieving comprehensive pollutant mineralization. Semiconductor photocatalysts have been the subject of considerable interest for a prolonged period due to their good photocatalytic performance and great potential in solving environmental problems. TiO_2 is the traditional photocatalyst demonstrated to be the most active among different semiconductor materials under the same conditions for the degradation of the same compound. However, its utilization is limited in the ultraviolet region because of its wide bandgap (3.2 eV).[11,12] Other widely explored semiconductors consist of Fe_2O_3,[13] graphene oxide,[9] graphene oxide–ZnO,[14] ZrO_2,[15] *etc.* The pristine semiconductors with low energy bandgap are expected to perform well under visible light irradiation but the fast recombination of photo-generated electrons and holes during the reaction process limits their applications.[16] Many studies have focused on materials with visible-light response based on mixed oxide semiconductors such as CuO/ZnO,[17] CuS/ZnS,[18] *etc.*, or metal-doped semiconductors such as metal ion-implanted TiO_2,[19] rare earth-doped ZnO,[20] vanadium and nitrogen co-doped TiO_2,[21] and so on. The combination of different metal oxides can transfer photo-generated electrons and holes from one semiconductor to another due to the formation of a heterojunction between two different bandgap semiconductors, thus decreasing the rate of electron–hole recombination leading to the improvement in the efficiency of the photocatalytic reaction.[22,23] The disparity in energy levels between the conduction band of one semiconductor and the valence band of another within the composite system is smaller than the bandgaps exhibited by each component. This characteristic may result in a shift of absorbed light wavelength towards the visible region.[24] To absorb solar light, semiconductors with bandgap energy larger than 3 eV must be modified by composite or doping to reduce the bandgap to below 3 eV. The large surface area of nanostructures gives rise to good photodegradation performance. The photocatalytic efficiency also depends on the ratio of two contents and the amount of photocatalyst in the reaction system.[25]

Zinc oxide (ZnO) exists in three crystal structures, namely, cubic rock salt, hexagonal Wurtzite, and cubic zinc blende.[26] The electronic structure of Zn^{2+} is $[Ar]3d^{10}4s^0$; the d-orbitals of Zn^{2+} in ZnO are partially filled and responsible for the photocatalytic properties of the semiconductor. ZnO inherently exhibits n-type semiconductor characteristics and has an impressive photocatalytic behavior, chemical stability, low-cost and non-toxic nature with a wide band gap of 3.2 eV and large exciton binding energy at 60 meV.[27] Its ultraviolet (UV) absorption capacity enables the complete mineralization of pollutants in wastewater, rendering it a cost-effective alternative compared to other photocatalysts.[28] Two limitations impacting the photocatalytic efficacy of ZnO include its limited resistance to charge carrier recombination and its wide bandgap, which preclude the effective utilization of visible light.[29] The challenges pertaining to ZnO can be mitigated through appropriate modifications in its surface or structure because the electronic properties of ZnO could be altered by impregnation/doping of impurities into their lattice structure or forming heterojunctions with other metal oxides.[30,31] Dopants create another energy level in the bandgap region, which results in the reduction of the bandgap, thereby shifting the light absorption wavelength to the visible region. Other methods for designing visible light-enabled photocatalysts are surface modification and metal deposition.[32,33] ZnO modified by other metal oxides such as TiO_2,[34–36] Fe_2O_3,[23,37–44] CuO,[45–51] Cu_2O,[52] WO_3,[53] *etc.*, or non-metals like g-C_3N_4,[16] polymer,[54] carbon black,[55] graphene oxide,[14] CdS,[56] or doped with noble metals/rare earth metals such as Au,[57] Ce,[58] Eu,[59] La, Nd, Sm, and Dy,[20] and so on, have been investigated to amplify their photocatalytic efficacy in the degradation of organic compounds under solar irradiation. The presence of oxygen vacancies and zinc interstitials renders doped-ZnO conducive to photocatalytic processes under visible light irradiation.[60] Although substantial progress has been made in developing highly effective ZnO-based photocatalysts, their practical implementation in industrial settings is still restricted.[61] An obstacle encountered in the process of doping metal/non-metal onto semiconductor structures is the generation of excess defect sites. The photocatalytic properties of ZnO have two significant drawbacks: first, due to its wide bandgap energy (~3.2 eV), only UV light can excite photo-generated charge carriers; second, the fast recombination between electrons and holes leads to a small number of reactive radicals in the photocatalytic process.[62] Therefore, it is necessary to enhance the quality of photocatalysts and heterogeneous photocatalytic technology, hence, the amalgamation of ZnO with alternative narrow bandgap semiconductors like CuO,[17,45–47,63] and Fe_2O_3 (ref. 4, 22, 23, 27, 37–39, 64 and 65) presents an opportunity to bolster light absorption within the visible wavelength range and extend the longevity of photo-excited charge carriers due to effective electron–hole separation.

Hematite (α-Fe_2O_3) is a binary oxide having a narrow bandgap of 2.1 eV and a visible-light-responsive semiconductor photocatalyst.[66] It is environmentally friendly, thermodynamically stable, and low-cost but is not an efficient photocatalyst

owing to its high recombination rate (<10 ps) of photogenerated electric charges. It can be used as a sensitizer under visible irradiation and as a donor if it is coupled with a wider bandgap semiconductor like ZnO. Numerous materials have been suggested in heterojunction configurations to enhance the efficiency when combined with Fe_2O_3, including other metal oxides (SnO_2, Cu_2O, NiO, TiO_2),[67–70] chalcogenides (MoS_2, CdS),[71,72] complex oxides ($BaTiO_3$),[73] *etc.* ZnO and Fe_2O_3 have emerged as mutually complementary metal oxides, presenting an apt hybridization option for photocatalytic utilization. O. E. Cigarroa-Mayorga has synthesized ZnO/Fe_2O_3 nanoparticles to degrade MB.[37] Harijan also studied ZnO/Fe_2O_3 nanoparticles for the degradation of MB.[38] Other morphologies of Fe_2O_3 in combination with ZnO include nanorods,[4,74] nanoflowers (for the degradation of MB and methyl orange, MO),[39] nanotubes,[42] and microspheres.[44] Table 1 outlines recent discoveries pertaining to ZnO/Fe_2O_3-based photocatalysts employed for the degradation of organic pollutants in wastewater. However, based on our review of the literature, the photocatalytic activity of the ZnO nanoplates/Fe_2O_3 nanospindles hybrid towards MB has not been investigated.

Hydrothermal processing represents a potent approach for fabricating transition metal oxides with customized morphologies and distinctive properties tailored to specific application needs.[81] In this investigation, we detail the synthesis and characterization of a hybrid photocatalyst combining ZnO nanoplates (NPls) and Fe_2O_3 nanospindles (NSs) with various weight ratios (ZnO : Fe_2O_3 = 2 : 5, 2 : 3, 1 : 1, 3 : 2, 5 : 2) through a facile hydrothermal route.

The results showed that the ZnO : Fe_2O_3 = 3 : 2 sample exhibited photocatalytic efficiency in the degradation of MB of 99.3% after 85 min of green light-emitting diode (GLED) illumination, which is the highest performance compared to other publications. The heterojunction between ZnO NPls and Fe_2O_3 NSs can augment the active surface area and reduce the recombination rate between electrons and holes. The photocatalytic performances of the synthesized ZnO NPls/Fe_2O_3 NSs composites were assessed through the breakdown of methylene blue (MB) in an aqueous medium under irradiation by green light-emitting diode (GLED) illumination. An investigation of the mechanism governing heterojunction formation, which is pivotal in shaping visible light photocatalytic behavior, was carried out. Consequently, an energy band diagram illustrating charge separation at the heterojunction interface has been proposed. The efficacy of the synthesized nanocomposite is significant in the advancement of photocatalytic technology, determining its feasibility for practical applications.

2. Experimental

2.1. Materials and chemicals

In this work, all the reactants and solvents were of analytical grade and applied without any additional refining. Zinc nitrate hexahydrate $Zn(NO_3)_2 \cdot 6H_2O$ (99%), potassium hydroxide (KOH, 85%), ferric chloride hexahydrate ($FeCl_3 \cdot 6H_2O$), sodium dihydrogen phosphate (NaH_2PO_4), methylene blue (MB, $C_{16}H_{18}ClN_3S$), and absolute ethanol (C_2H_5OH) were purchased from Merck (Germany) for use in the synthesis and photocatalytic measurements. Double distilled water was used as a solvent during the solution preparation and as a cleaner for all glassware.

2.2. Synthesis of ZnO nanoplates

The ZnO nanoplates were prepared by a hydrothermal method. Firstly, certain quantities of $Zn(NO_3)_2 \cdot 6H_2O$ and KOH were dissolved in distilled water under continuous stirring to obtain 0.5 M $Zn(NO_3)_2$ and 1.5 M KOH solutions (Fig. 1a). KOH was added drop-wise into the $Zn(NO_3)_2$ solution until the $Zn(NO_3)_2$: KOH molar ratio of 1 : 2 was achieved under vigorous stirring for 15 minutes at room temperature to obtain a white milky $Zn(OH)_2$ precipitate. Subsequently, the resultant mixture solution was encapsulated within a Teflon-coated stainless-steel autoclave and exposed to heating at 180 °C for 20 hours. After naturally cooling to room temperature, the white precipitates were separated *via* filtration and meticulously cleansed with

Table 1 ZnO/Fe_2O_3-based photocatalysts for the photodegradation of organic pollutants

Materials	Synthesis method	Pollutants	Performance	Year (Ref.)
ZnO/Fe_2O_3 nanoparticles	Sol–gel	Potassium cyanide	—	2007 (ref. 44)
Fe_2O_3/ZnO core–shell	Microwave hydrothermal	Methyl orange	70% at 140 min	2011 (ref. 75)
ZnO/Fe_2O_3 nanoparticles	Hydrolysis	Salicylic acid	64% at 60 min	2014 (ref. 23)
ZnO/Fe_2O_3 spheres	Sol–gel	Dichlorophenoxyacetic acid	47% at 330 min	2015 (ref. 76)
ZnO/Fe_2O_3 nanotubes	Photochemical deposition	Methylene blue	94.25% at 60 min	2015 (ref. 42)
ZnO/Fe_2O_3 spindles	Chemical route	Pentachlorophenol	—	2015 (ref. 77)
Fe_2O_3/ZnO flowers	Chemical reaction	Pentachlorophenol	54.6% at 4 h	2015 (ref. 29)
ZnO/Fe_2O_3 nanosheets	Hydrothermal	Cefixime trihydrate	99.1% at 127 min	2017 (ref. 22)
ZnO/Fe_2O_3 spheres	Co-precipitation	Victoria blue	100% at 8 h	2017 (ref. 78)
ZnO/Fe_2O_3 spheres	Flocculation	Orange II	74.8% at 120 min	2019 (ref. 79)
Fe_2O_3/ZnO nanoparticles	Solvothermal	GRL dye	81.1% at 200 min	2019 (ref. 40)
ZnO/Fe_2O_3 flowers	Microwave	Tetracycline	88% at 150 min	2020 (ref. 80)
Fe_2O_3/ZnO nanowires	Electrodeposition	Methylene blue	91.07% at 180 min	2022 (ref. 37)
ZnO/Fe_2O_3 nanoparticles	Chemical method	Methylene blue	—	2022 (ref. 38)
ZnO/Fe_2O_3 nanorods	Self-aggregation	Azo dye	98% at 180 min	2022 (ref. 4)

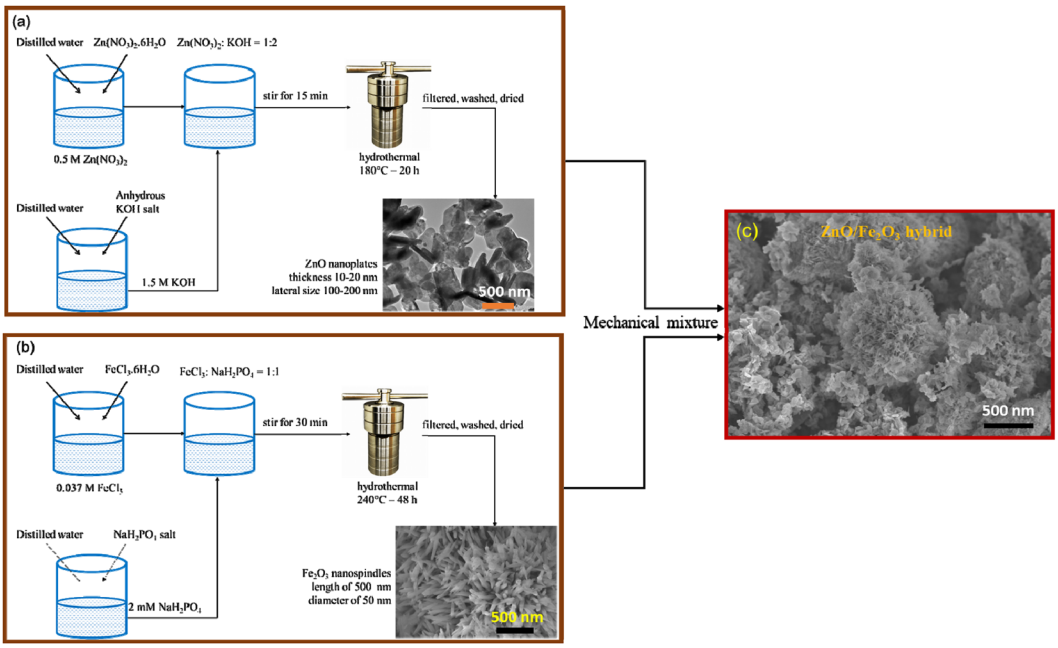

Fig. 1 Schematic of the preparation of (a) ZnO nanoplates, (b) Fe_2O_3 nanospindles, and (c) ZnO/Fe_2O_3 hybrid materials.

distilled water and absolute ethanol several times to complete the eradication of nitrate and potassium ions. The washed precipitate was finally dried overnight in an electric oven at 80 °C, which resulted in a white powder.

2.3. Synthesis of Fe_2O_3 nanospindles

To prepare Fe_2O_3 nanospindles, the hydrothermal synthesis technique was employed based on a method described in a prior publication[82] (Fig. 1b). The precursors, ferric chloride hexahydrate ($FeCl_3 \cdot 6H_2O$) and sodium dihydrogen phosphate (NaH_2PO_4), were dissolved in water separately and mixed in a 50 ml beaker with molar ratio of 1 : 1 under continuous stirring for 30 min, resulting in a yellowish iron hydrate $Fe(OH)_3$ precipitate. The obtained mixture was hydrothermally treated at 240 °C for 48 h. After naturally cooling down to room temperature, the red-brown precipitate was isolated *via* filtration, washed multiple times with deionized water and ethanol to remove the residuals, and subsequently dried overnight at 80 °C, resulting in a red hematite powder.

2.4. Synthesis of ZnO/Fe_2O_3 composites

For the preparation of the ZnO/Fe_2O_3 nanocomposite, the appropriate amounts of ZnO powder and Fe_2O_3 powder according to five weight ratios (*i.e.*, 2 : 5, 2 : 3, 1 : 1, 3 : 2, and 5 : 2) were together dispersed in double-distilled water using a magnetic stirrer for 2 hours. The resultant product was dried at 80 °C in an air oven for 12 hours.

2.5. Characterization

The structural features of the as-prepared samples were characterized by powder X-ray diffraction (XRD) analysis (Bruker D8 Advance diffractometer, Germany) using CuK_α radiation (X-ray wavelength of $\lambda = 0.154056$ nm) and 2θ scanning angles ranging from 20° to 80° with a scan rate of 0.05° s^{-1}. The microstructure and surface morphology were accessed *via* field emission scanning electron microscopy (FESEM, Hitachi S4800, Japan) operating at an acceleration voltage of 20 kV and transmission electron microscopy (TEM, Philips CM-200, Japan) operating at 200 kV. Energy-dispersive X-ray spectroscopy (EDS) was performed on a Hitachi SU 8020 at an elevated voltage of 200 kV for elemental quantification. The optical properties were estimated using UV-vis absorption spectra recorded on a Jasco V-770 spectrophotometer in the 200–1400 nm wavelength range to examine their bandgap energies. The zeta potential was measured through electrophoresis on the commercial Zetasizer (MAL 1062724, Malvern Instruments Ltd) at 25 °C using water as a dispersant. All the characterization measurements mentioned above were carried out at room temperature.

2.6. Photocatalytic performance measurements

The photocatalytic performances of ZnO nanoplates, Fe_2O_3 nanospindles, and ZnO/Fe_2O_3 nanocomposites were studied by using an aqueous solution of MB as the organic dye. Here, 50 ml of MB aqueous solution with an initial concentration of 10 ppm was prepared by dissolving 0.5 mg MB in 50 ml of doubly distilled water. The pH of the solution was kept at 7. Photocatalytic assessments were carried out at ambient temperature within a 100 ml beaker containing 12.5 mg catalyst powder and 50 ml MB solution. Preceding illumination, the mixture underwent continuous stirring under dark conditions for 1 h at room temperature to attain equilibrium of the absorption and desorption processes between MB and the photocatalyst. The subsequent degradation of MB was investigated in the green light-emitting diode (GLED) with radiation at a wavelength of

520 nm and a power intensity of 0.5 mW cm^{-2} within an enclosed chamber. The distance between the solution and the light source was approximately 10 cm. The photocatalytic experiment was carried out for 240 min. Here, 2 ml of suspension containing MB and powder catalyst were extracted at given time intervals to determine the residuary MB concentration and the reaction rate using a UV-vis spectrophotometer (Jasco V-770) at the maximum peak of 664 nm. The calibration curve was prepared from the MB concentration and illuminating time. To estimate the effect of the $ZnO : Fe_2O_3 = 3 : 2$ sample amount on photocatalytic efficiency, different catalyst dosages were used: 0.1, 0.15, 0.2, 0.25, 0.3, 0.35, and 0.4 g l^{-1}. The efficiency of MB degradation at time t was estimated using the following equation:[83]

$$\eta(\%) = \frac{C_o - C_t}{C_o} \times 100 \quad (1)$$

where C_o and C_t are the initial concentration of MB and MB concentration at time t, respectively.

A blank MB solution (without catalyst) was also subjected to the same conditions to exhibit the role of the photocatalyst in MB degradation. To investigate the effect of pH value on the MB degradation efficiency of the $ZnO : Fe_2O_3 = 3 : 2$ hybrid sample, acetic acid (CH_3COOH) solution, and sodium hydroxide (NaOH) solution were used to modify the acidic or basic properties of the MB solution. The two pH values chosen were 3 and 9.54. For each reaction time, the final results were averaged out of three independent experiments. To investigate the recycling stability of the nanocatalyst, the $ZnO : Fe_2O_3 = 3 : 2$ sample was reused for MB photodegradation after being magnetically separated.

3. Results and discussion

3.1. X-ray diffraction and phase analysis

X-ray diffraction (XRD) analysis was performed to identify the crystalline structure and phase purity of the obtained samples. The XRD patterns of ZnO, Fe_2O_3, and ZnO/Fe_2O_3 with various weight ratios of 5 : 2, 3 : 2, 1 : 1, 2 : 3, 2 : 5 are shown in Fig. 2. The major peaks of the wurtzite structure of ZnO appeared at 2θ values of 31.74°, 34.4°, 36.3°, 47.6°, 56.6°, 62.9°, and 68°, corresponding to the crystalline planes of (100), (002), (101), (102), (110), (103), and (112), respectively (Fig. 2a). All these reflections are in complete agreement with the standard XRD pattern of the hexagonal wurtzite structure (JCPDS card No.: 36-1451). The XRD lines are fairly narrow, indicating the good crystallinity of ZnO, with no secondary impurity detected. The XRD pattern of the Fe_2O_3 sample shows peaks at 2θ of 21.5°, 33.2°, 36.1°, and 53.9°, corresponding to the (012), (113), (110), and (116) crystalline planes, respectively, and indicates the formation of the rhombohedral Fe_2O_3 structure, in good agreement with JCPDS card No. 33-0664. The XRD patterns of ZnO/Fe_2O_3 composites clearly indicate mixed phases (Fig. 2b), where the reflections of ZnO are distinctly observable and the reflections from Fe_2O_3 nanospindles are substantially lower due to the shielding by ZnO nanoplates. With the increasing weight ratio of Fe_2O_3 : ZnO, the peak intensity of the Fe_2O_3 phase increased due to the growth of Fe_2O_3 crystals. Moreover, no shift in ZnO peak position was observed with increasing the Fe_2O_3 content. This indicates no change in the structure of ZnO in the hybrid process. In addition, no diffraction peaks from any other impurities were observed. The average crystallite sizes were evaluated from the full width at half maximum of the most intense diffraction peak (Fig. 2c) according to the Scherrer equation:[17]

$$D = \frac{k\lambda}{\beta \cos \theta} \quad (2)$$

where D is the average crystallite size, $k = 0.893$ is the Scherrer constant, $\lambda = 0.154056$ nm is the X-ray wavelength, β is the full width at half maximum (FWHM) of the diffraction peak, and θ is the Bragg diffraction angle. Based on the highest peak at 36.3°, the evaluated crystallite size of ZnO was 23.69 nm. The crystallite size of Fe_2O_3 was obtained from the 36.1° peak to be 8.3 nm. The crystallite sizes of pure ZnO nanoplates, pristine Fe_2O_3 nanospindles, and the ZnO/Fe_2O_3 hybrid with different weight ratios of $ZnO : Fe_2O_3$ are shown in Fig. 2d and Table 2. The $ZnO : Fe_2O_3 = 3 : 2$ sample possesses the largest crystallite size of 28.6 nm.

3.2. Morphology, size, and composition

The SEM image of ZnO presented in Fig. 3a exhibits a two-dimensional (2D) plate-like structure with high concentration, uniformity in size, and regular shape. The high magnification TEM image in Fig. 3b reveals that the nanoplates with smooth surfaces are about 20 nm in thickness and 100 × 200 nm in lateral dimensions.

Fig. 3c shows that the Fe_2O_3 nanospindles are regular with a narrow size distribution. Their length and width are about 500 nm and 50 nm, respectively. The low magnification SEM image of ZnO/Fe_2O_3 with a weight ratio of 3 : 2 in Fig. 3d demonstrates that the composite retains the initial structure of the ZnO nanoplates and Fe_2O_3 nanospindles. The Fe_2O_3 nanospindles made contact with the surface of the ZnO nanoplates to form the desired heterojunction. It can be concluded that a homogeneous ZnO/Fe_2O_3 nanocomposite with interconnectivity was formed by mechanical mixing. The large cauliflower with a diameter above 500 nm appeared as the aggregates of the smaller nanospindles (Fig. 3e).

Fig. 4a displays the EDS spectrum of the ZnO/Fe_2O_3 hybrid with strong peaks corresponding to three elements of O, Fe, and Zn that confirmed the successful preparation of the composite. It also shows the percentage composition of each element. No impurities were observed, which confirmed the purity of the composite.

3.3. Bandgap energy

Analysis of the effective absorption edge of the samples was carried out using UV-vis optical absorption spectroscopy. The UV-vis absorption spectrum of pristine ZnO NPls was reported in our previous publication.[17] Pure ZnO exhibited a singular, well-defined absorption edge around 380 nm, attributable to the charge-transfer process from the valence band to the conduction band of ZnO.[84] In ZnO, the valence band is

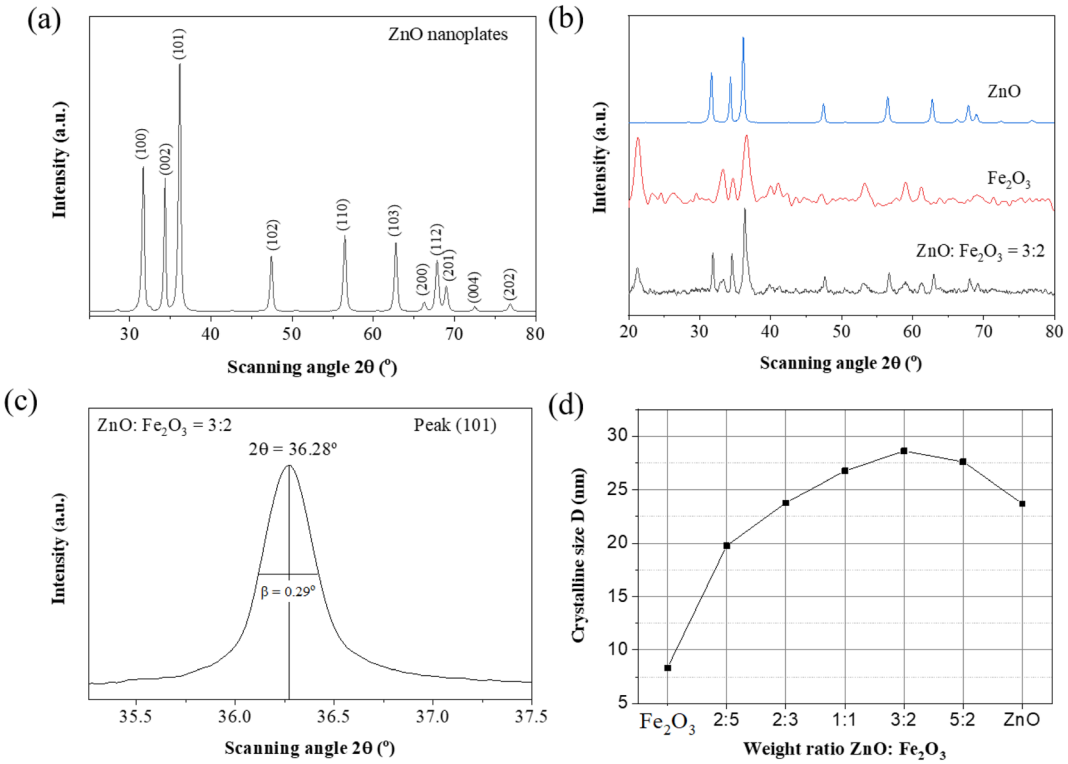

Fig. 2 (a) XRD patterns of ZnO nanoplates. (b) Comparison of the XRD patterns of pure ZnO, pristine Fe_2O_3 nanospindles and ZnO/Fe_2O_3 hybrids with a ZnO : Fe_2O_3 weight ratio of 3 : 2. (c) The full width at half maximum of a diffraction peak and Bragg diffraction angle; (d) the dependence of crystallite size on the ZnO : Fe_2O_3 weight ratio.

Table 2 The crystallite sizes of various samples calculated from the Scherrer equation

Sample	Fe_2O_3	ZnO	2 : 5	2 : 3	1 : 1	3 : 2	5 : 2
D (nm)	8.3	23.69	19.75	23.78	26.75	28.6	27.6

composed of 2p orbitals of O^{2-} ions, while the conduction band is composed of 4s orbitals of Zn^{2+} ions. This means ZnO solely absorbs light within the ultraviolet (UV) range. For pure Fe_2O_3, the strong absorption was observable in the visible region (~550 nm), in which, the valence band is formed from 2p orbitals of O^{2-} ions and the conduction band from 3d orbitals of Fe^{3+} ions. The UV-vis spectrum of the ZnO/Fe_2O_3 sample comprises two adsorption edges. The low energy edge is observed in the visible range of 500–580 nm, which is ascribed to the Fe_2O_3 content. The higher energy edge is observed in the ultraviolet range of 380–400 nm, which is assigned to the ZnO content (Fig. 5a). The emergence of two distinct band edges in the UV-vis spectra of the ZnO/Fe_2O_3 hybrid confirmed the successful formation of the nanocomposite. To calculate the optical bandgap energy (E_g) of the samples, we used the relationship between the absorption coefficient (α) and photon energy of the exciting light ($h\nu$) according to Tauc's law:[85]

$$(\alpha h\nu)^n = A(h\nu - E_g) \quad (3)$$

where A is a constant, h is Planck's constant, ν denotes the light frequency, $n = 2$ for direct bandgap, and $n = 0.5$ for indirect bandgap, respectively. In this case, n is equal to 2 due to the direct bandgap energy of ZnO.[86] Fig. 5b exhibits the Tauc plots, with $(\alpha h\nu)^2$ along the Y-axis as a function of $h\nu$ (photon energy) in eV along the X-axis. The optical bandgap energy (E_g) values of the samples can be evaluated from the intercept of the tangent of the linear region of the Tauc plots with the abscissa axis. The estimated bandgap values of bare ZnO and Fe_2O_3 are 2.8 eV, and 1.6 eV, respectively. These bandgap values in mixed oxides are lower than those of corresponding contents. These results are closer to those reported for ZnO and ZnO/Fe_2O_3 in the literature.[44,87] The red shift in the bandgap energy values with increasing the Fe_2O_3 content can be explained by the lower bandgap of Fe_2O_3 compared to ZnO and the interaction between Fe_2O_3 and ZnO. This is in agreement with previous studies on the bandgap energy of ZnO/Fe_2O_3 nanocomposites.[22,23] This suggests that the incorporation of Fe_2O_3 can significantly enhance the visible-light responsiveness of ZnO, thereby enabling the utilization of sunlight as an energy source for photocatalytic reactions.

The charge on the particle surface generates electrostatic forces and the zeta potential represents the intensity of electrostatic interactions and the nature of the surface charge. The zeta potential related to the electrostatic potential generated by the ZnO/Fe_2O_3 heterojunction for the ZnO : Fe_2O_3 = 3 : 2 sample in neutral media (pH = 7) is shown in Fig. 6. Three zeta

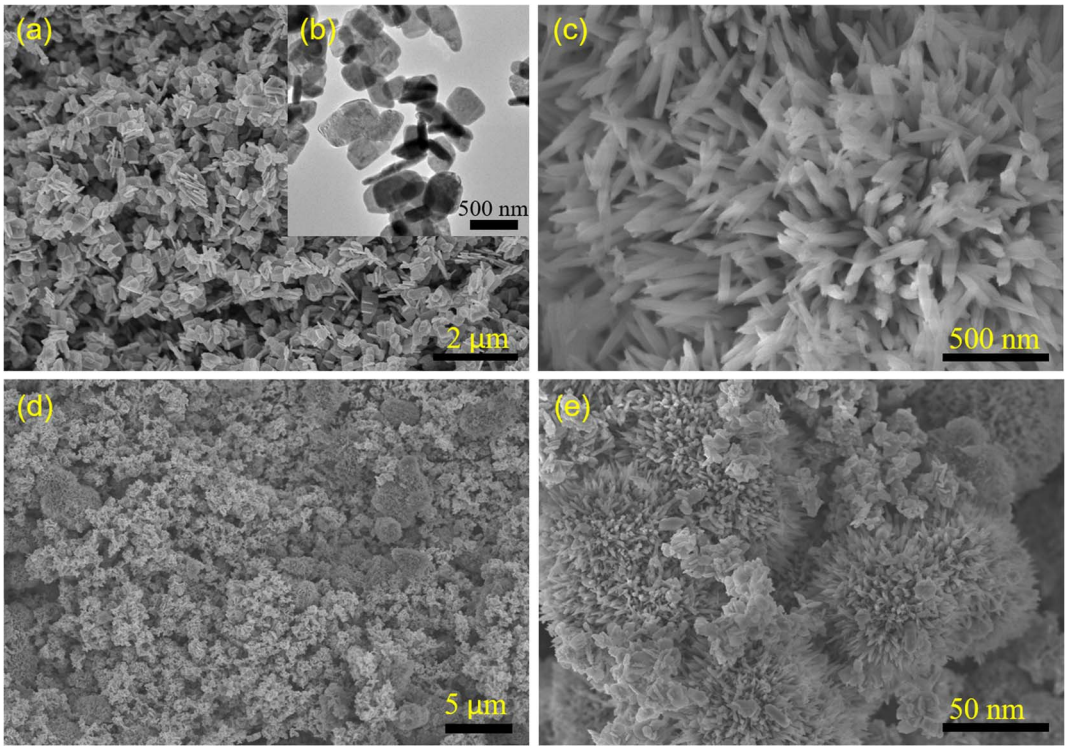

Fig. 3 (a) SEM image of ZnO, (b) TEM image of ZnO, (c) SEM image of Fe_2O_3, and SEM images of ZnO/Fe_2O_3 with magnifications of (d) 2,000, and (e) 10 000.

potential values were −108, −87.2, and −60.9 mV, indicating the negative surface charge of Fe_2O_3, and the surface of the ZnO/Fe_2O_3 nanocomposites was homogeneous.

3.4. Photocatalytic activity

3.4.1. Comparison of the photocatalytic activities of the as-synthesized photocatalysts. Background analysis conducted in the absence of a catalyst indicated the negligible degradation of methylene blue (MB) resulting from direct photolysis. Fig. 7a indicates that the concentration of MB solution was 99.8% of the initial concentration after 85 min of GLED illumination, and this suggests that the photocatalytic degradation of MB in the presence of visible light is very weak. The subsequent immersion of catalysts into the solution significantly heightened the degradation efficiency of MB. Also, MB adsorption on the ZnO, Fe_2O_3, and ZnO/Fe_2O_3 composites in the dark was evaluated at lower than 5%. The photocatalytic degradation of MB dye was performed under GLED light (wavelength of 520 nm) for 85 min with a catalyst dosage of 0.25 g l^{-1} and an initial MB concentration of 10 ppm. The decolorization process was quantified by measuring the decrease in the intensity of the 664 nm peak in the UV-vis spectra. Fig. 7 (b–h) displays the degradation efficiency of MB over different samples *versus* illumination time. The intensity of the absorption peak decreased with time while the band position did not shift

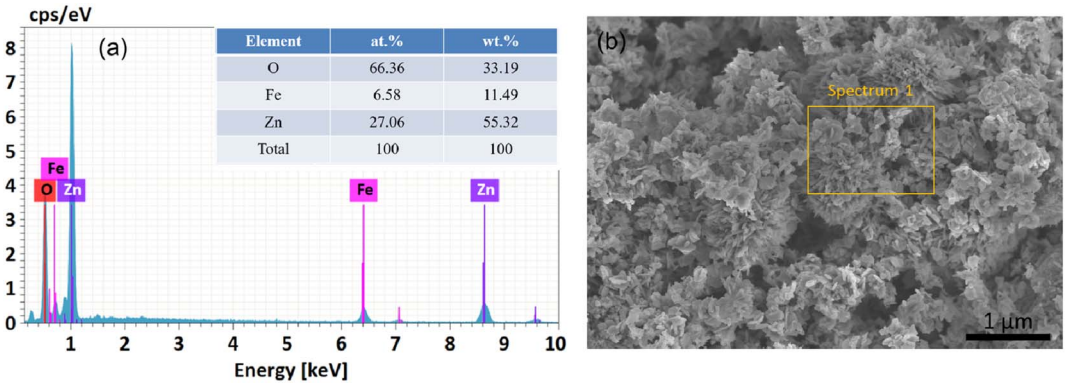

Fig. 4 (a) The energy-dispersive X-ray spectrum (EDS) of the ZnO : Fe_2O_3 = 3 : 2 hybrid, and (b) the corresponding area of the SEM image.

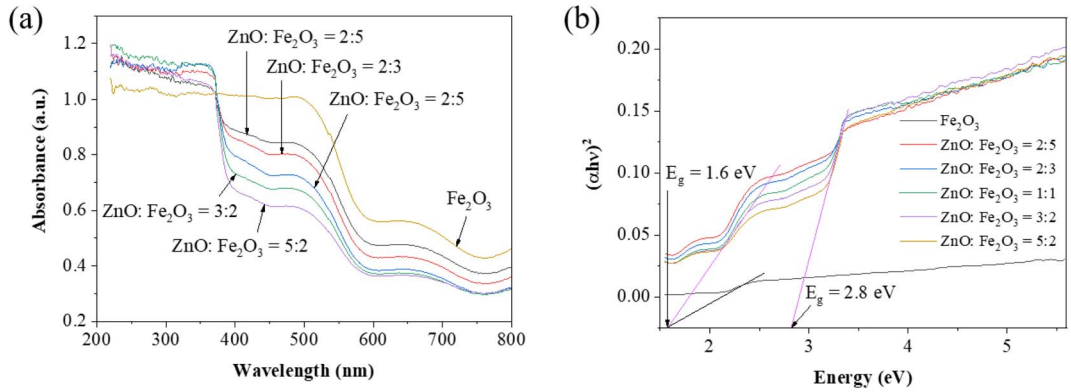

Fig. 5 (a) UV-vis absorption spectra of pure Fe_2O_3 nanospindles and ZnO/Fe_2O_3 nanocomposites. (b) Tauc's plots derived from corresponding UV-vis spectra.

during the photodegradation. For pure ZnO nanoplates, 95.7% of the MB was degraded after 85 min of irradiation (Fig. 7b).

The pristine Fe_2O_3 sample shows the minimum photocatalytic activity among all the samples (degradation of 88.3% after 85 min) (Fig. 7c). All the ZnO/Fe_2O_3 heterostructures exhibited significantly improved photocatalytic efficacy. The photocatalytic efficiency of different photocatalysts towards the degradation of MB was evaluated at 85 min GLED illumination (Fig. 7d–h). The degradation capacity decreased in the sequence of 3 : 2 > 5 : 2 > 1 : 1 > 2 : 5 > 2 : 3 > ZnO > Fe_2O_3. Fig. 7h shows the UV-vis absorption spectra of the MB solution (initial concentration of 10 ppm) before GLED illumination using pure ZnO or pristine Fe_2O_3 as catalysts.

Fig. 8a shows the decrease in MB concentration under GLED illumination for 0–85 min using different photocatalysts. Fig. 8b indicates the photocatalytic efficiencies of various photocatalysts after the same illumination time. The ZnO : Fe_2O_3 = 3 : 2 sample represents 99.3% photocatalytic efficiency within 85 min. However, a further increase in the amount of ZnO to 5 : 2 led to excessive agglomeration and poor heterojunction characteristics, which decreased the photocatalytic efficiency. According to Table 3, the ZnO nanoplates/Fe_2O_3 nanospindles hybrid demonstrated a greater photocatalytic performance in MB degradation compared to previous publications.

Fig. 8c illustrates the variation in the MB relative concentration (C_t/C_o) over time under GLED irradiation in the presence of samples, where C_o represents the initial concentration of MB and C_t denotes the concentration at different time intervals. Significantly greater amounts of MB are decomposed in the solutions with ZnO/Fe_2O_3 samples under the same conditions. The time-dependent photo-degradation of MB was fitted with the pseudo-first-order kinetic model:[91]

$$\ln\frac{C_o}{C_t} = kt \quad (4)$$

where k depicts the MB degradation rate constant. k is the slope of the straight-line $\ln(C_o/C_t)$ *versus* t (Fig. 8d), and provides the direct measurement of the degradation capacity of the photocatalysts in accordance with the literature.[92]

Table 4 exhibits the photocatalytic rate constants of different samples. The ZnO : Fe_2O_3 = 3 : 2 sample exhibited the highest rate constant, which is approximately 1.31 times greater than that of the pristine ZnO nanoplates and ~2.68 times that of the pristine Fe_2O_3 sample.

3.4.2. Effect of photocatalyst load. The photocatalyst dosage in the photocatalytic application was investigated at seven values of 0.1, 0.15, 0.2, 0.25, 0.3, 0.35, and 0.4 g l^{-1}. Fig. 9a and b shows the MB degradation efficiency by the ZnO : Fe_2O_3 =

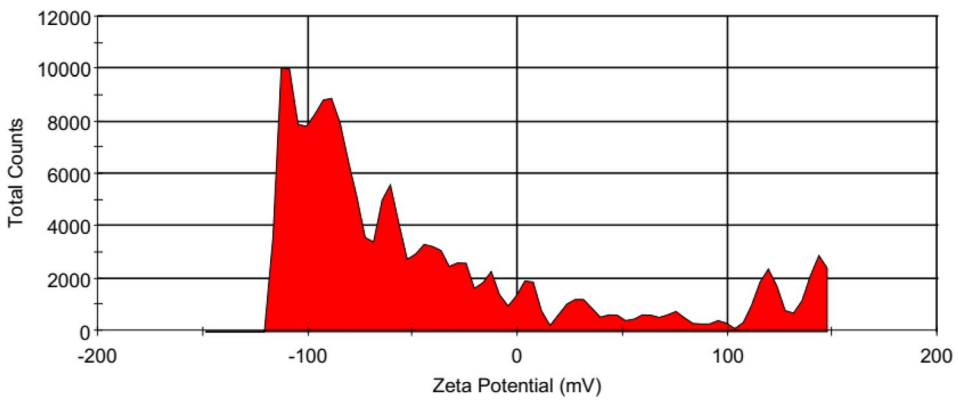

Fig. 6 Zeta potential distribution of the ZnO : Fe_2O_3 = 3 : 2 sample.

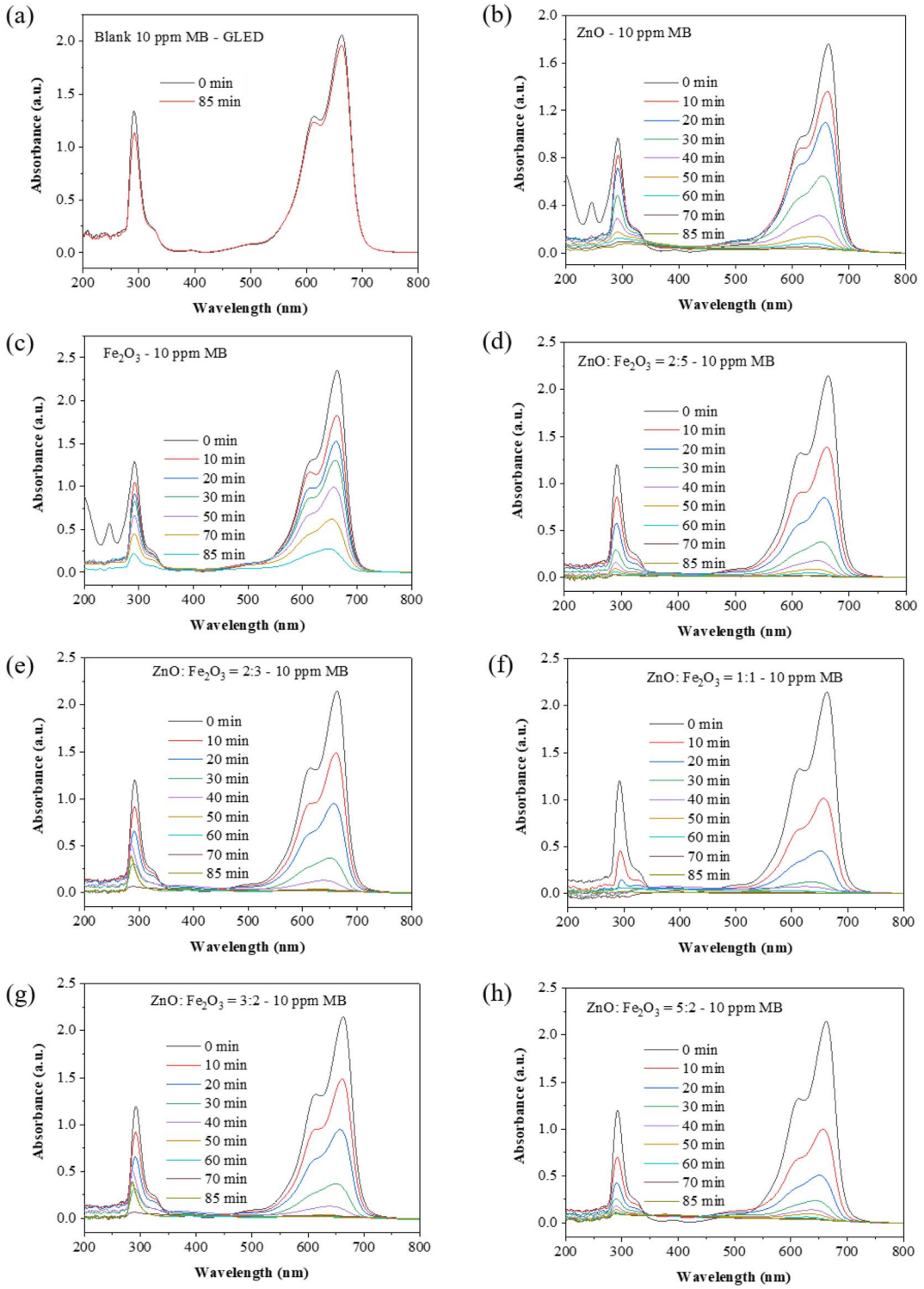

Fig. 7 UV-vis absorbance spectra of (a) the blank 10 ppm MB solution without a catalyst before and after GLED illumination for 85 min; (b) pure ZnO; (c) pristine Fe_2O_3; and ZnO/Fe_2O_3 with different ZnO : Fe_2O_3 weight ratios of (d) 2 : 5, (e) 2 : 3, (f) 1 : 1, (g) 3 : 2, and (h) 5 : 2 under GLED illumination for 0–85 min.

3 : 2 sample at these photocatalyst dosages. The highest photocatalytic efficiency was obtained at 0.25 g l^{-1}, which can be attributed to the greater abundance of active sites and charge carriers. Applying an extra dosage of the ZnO : Fe_2O_3 = 3 : 2 photocatalyst above 0.25 g l^{-1} reduced the photo-degradation efficiency because the excessive photocatalyst prevented light from reaching the surface of the nanocomposite.

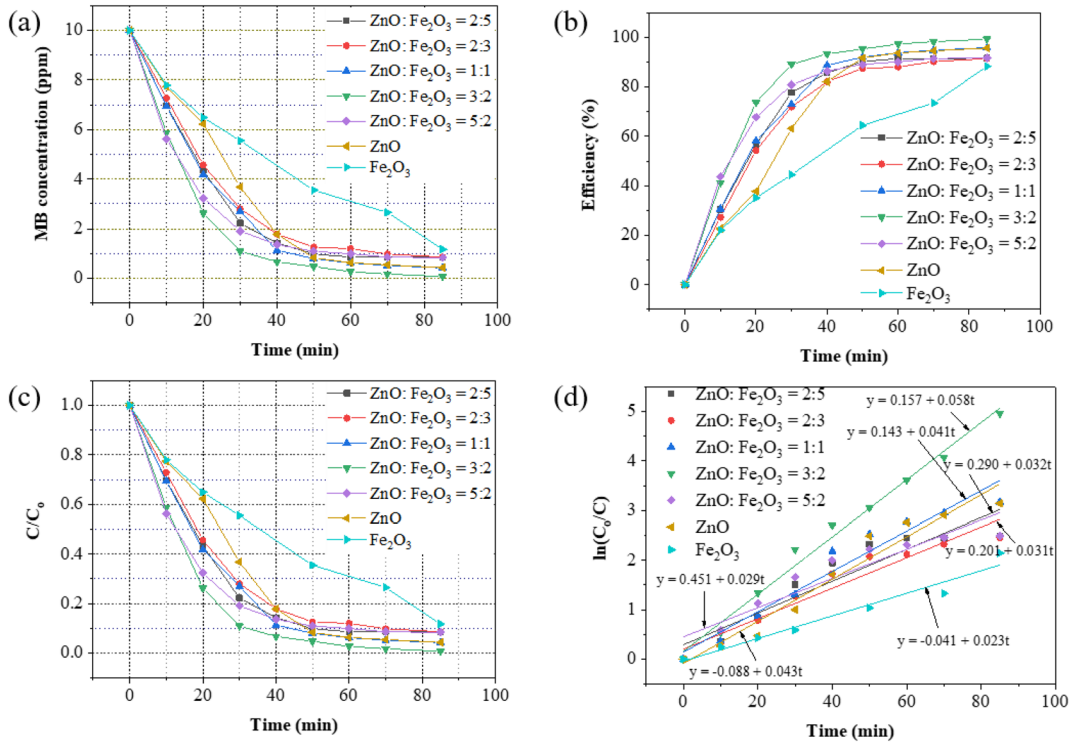

Fig. 8 (a) The dependence of MB concentration on the irradiation time of different samples, (b) the photocatalytic efficiency of different samples, (c) the dependence of C/C_o on irradiation time, and (d) the photocatalytic degradation rate of different samples.

Table 3 Comparison of recent reports on MB photodegradation performance of ZnO nanocomposites[a]

Photocatalyst	Light – time	Efficiency	Ref.
ZnO NWs/Fe_2O_3 NPs	UV – 180 min	91.07%	37
g-C_3N_4/ZnO/Fe_2O_3	Vis – 120 min	94%	88
NiO/ZnO/Fe_2O_3	Vis – 22 min	96.59%	89
ZnO/Fe_2O_3 NTs	UV – 60 min	94.25%	90
ZnO/CuO	Vis – 30 min	54%	63
ZnO NPls/Fe_2O_3 NSs	Vis – 85 min	99.3%	This work

[a] NPs = nanoparticles, NTs = nanotubes.

Table 4 The photocatalytic rate constants of different samples

Sample	ZnO	2 : 5	2 : 3	1 : 1	3 : 2	5 : 2	Fe_2O_3
k (min^{-1})	0.045	0.035	0.033	0.043	0.059	0.032	0.022

The active sites and the performance of the photocatalyst increase with the increase in photocatalyst dosage, but the performance declines if the dosage is beyond a certain concentration because the photons are screened by the excess catalyst. This experiment showed that with an increase in the ZnO/Fe_2O_3 (weight ratio of 3 : 2) dosage up to 0.25 g l^{-1}, the degradation efficiency of MB reached the maximum value, and the photocatalyst showed the best performance. Further increments in dosage gradually decreased the degradation rate because greater amounts blocked the light penetration (Fig. 9). These findings are in agreement with previous works.[93,94] It was concluded that the optimum weight ratio of ZnO : Fe_2O_3 was 3 : 2 and the optimum amount of photocatalyst was 0.25 g l^{-1} (weight of photocatalyst/volume of MB solution).

3.4.3. The effect of the solution pH. The solution pH significantly affects the photocatalytic reaction. Fig. 10 shows the effect of pH, ranging from 3 to 9.54, on the degradation of 10 ppm MB by the ZnO : Fe_2O_3 = 3 : 2 photocatalyst under visible light. The UV-vis absorbance spectra of 50 ml of MB dye solution in the presence of 0.25 g l^{-1} of the ZnO : Fe_2O_3 = 3 : 2 photocatalyst when the pH value of the solution was set at 3 (acidic medium), 7 (neutral medium), and 9.54 (basic medium) are presented in Fig. 10a–c, respectively. Fig. 10c shows that the MB degradation efficiency increased from 66.9% to 99.3% from pH 3 to 7 and decreased to 97.64% at pH 9.54 after 80 min of exposure. Fig. 10d displays the pseudo-first-order kinetics of MB degradation with ZnO : Fe_2O_3 = 3 : 2 in various media. The MB dye degradation profiles are well-defined by the kinetic constants of 0.016, 0.0578, and 0.0506 min^{-1} with the correlation coefficients (R^2) of 0.994, 0.988, and 0.993 at pH of 3, 7, and 9.54, respectively. The maximum MB degradation was observed in a near-neutral medium (pH 7) and complete degradation of MB was observed within 85 min of photocatalytic reaction under GLED light. Fascinatingly, the MB degradation rate at pH 7 was 3.6 times higher than that at pH 3. The degradation efficiency of MB in the alkaline medium was higher than that in the acidic medium. Beyond pH 7 (pH 9.54), although $^{\bullet}OH$ production in alkaline solution is higher than in acidic and neutral conditions, the negatively charged OH^- ions surround

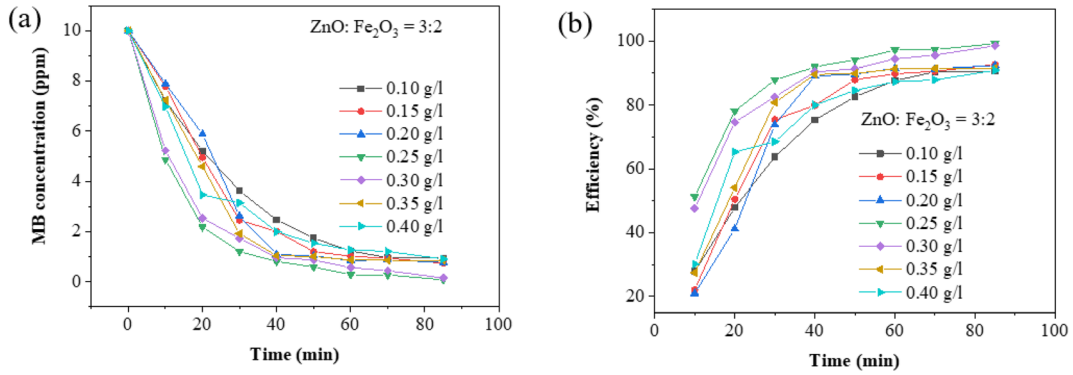

Fig. 9 (a) The dependence of MB concentration on the irradiation times of different amounts of the ZnO : Fe_2O_3 = 3 : 2 sample; (b) a comparison of the photocatalytic efficiencies of different amounts of the ZnO : Fe_2O_3 = 3 : 2 sample.

the catalyst surface and oppose MB molecules, decreasing the rate of dye degradation. In contrast, at lower pH (pH 3), the positively charged surface of the photocatalyst attracts the negatively charged MB molecules, and MB adsorption onto catalyst surface increases. However, the lower availability of OH^- ions to form highly active $^{\bullet}OH$ radicals led to a decrease in the degradation efficiency. Another reason behind the low degradation of MB at pH 3 may be the instability of ZnO and Fe_2O_3 in acidic conditions.[95] This result is in agreement with a previous report.[88] Therefore, acidifying or basifying the MB solution before photodegradation is unnecessary.

The ability to reuse the ZnO/Fe_2O_3 nanocomposite was assessed by performing consecutive photocatalytic degradations of MB after removing degradation by-products on the catalyst surface from active sites. The results of these experiments show that the photocatalytic efficiency decreases slightly with the number of cycles as shown in Fig. 11. This may be due to the loss of nanocatalyst during multiple washings and separations. It was concluded that the catalytic activity was preserved in the subsequent uses after five cycles. The recyclability test indicated that the ZnO/Fe_2O_3 photocatalyst displayed high stability.

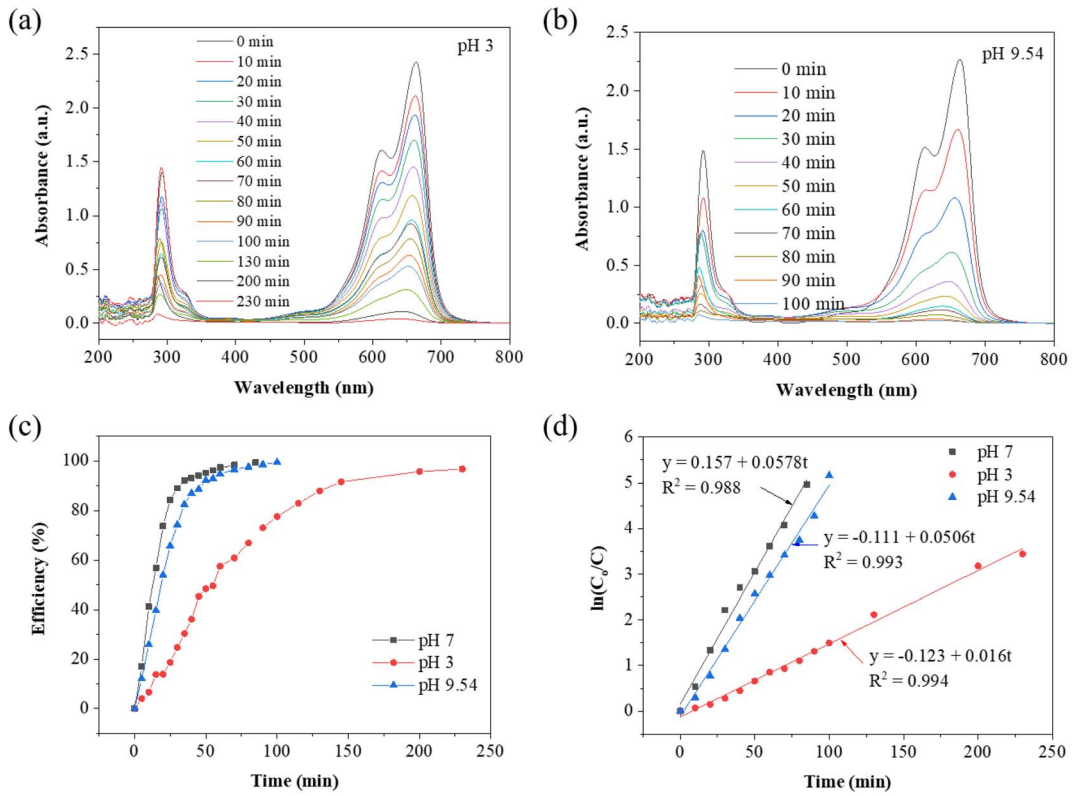

Fig. 10 The impact of solution pH on the photocatalytic activity of the ZnO : Fe_2O_3 = 3 : 2 sample at (a) pH 3 and (b) pH 9.54; the dependence of the photocatalytic efficiency (c) and ln(C_o/C) (d) on illumination time with an initial MB concentration of 10 ppm.

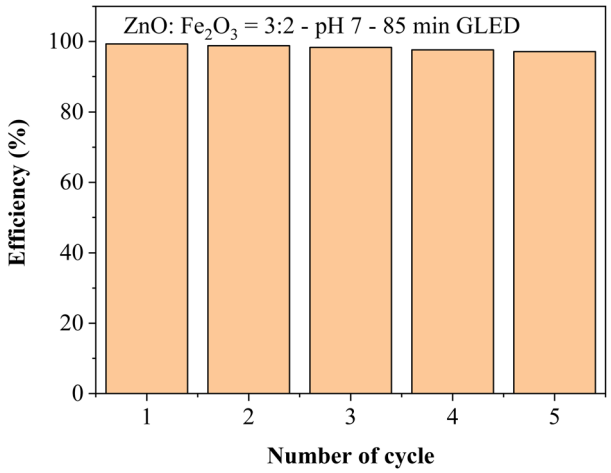

Fig. 11 The recyclability of the ZnO : Fe_2O_3 = 3 : 2 sample at pH 7 towards 10 ppm MB after 5 cycles.

3.5. Photocatalytic mechanism

The photocatalysis reaction is initiated by the absorption of photons from the light source by a photocatalyst. The photon energy must be greater than the bandgap energy of the photocatalyst to produce electron and hole pairs due to the migration of electrons from the valence band to the conduction band. In the context of photodegradation, a notable challenge arises from the phenomenon of electron–hole recombination, which impedes the efficiency of the degradation process. Efficient charge carrier separation is an important factor for enhancing photocatalytic activity, therefore, the enhanced photocatalytic performance of the ZnO/Fe_2O_3 hybrid can be ascribed to this. One possible reason for the relatively low visible light activity of Fe_2O_3 is that the bandgap energy of Fe_2O_3 is narrow, which leads to a fast recombination rate, so the amount of photoinduced charge carriers is not enough to oxidize H_2O to $^{\bullet}OH$ reactive radicals and reduce O_2 to $^{\bullet}O_2^-$ reactive radicals.[96] The lack of active sites on the surface of Fe_2O_3 nanospindles may be another explanation for the low photocatalytic performance of pristine Fe_2O_3. However, in the ZnO/Fe_2O_3 nanocomposite, Fe_2O_3 plays the role of a visible light absorbent to generate photoinduced electrons and holes and forms a heterostructure with ZnO. The Fermi level of ZnO is 1.47 eV, which is higher than that of Fe_2O_3 (1.38 eV),[83] so electrons in the CB of ZnO get transferred into the CB of Fe_2O_3. The VB of Fe_2O_3 is situated midway between the CB and VB of ZnO, so holes in the VB of Fe_2O_3 are transferred into the VB of ZnO. This indicates that Fe_2O_3 can function as a reservoir for photo-generated electrons and ZnO acts as a sink for photo-generated holes, which increase the electron–hole separation efficiency, decrease the recombination rate of photo-induced e^-/h^+ and prolongs the lifetime of charge carriers.[29] The intrinsic defect sites on the surface of ZnO/Fe_2O_3 nanocomposites trap the photo-excited charge carriers. Oxygen vacancies in ZnO can act as sub-bandgap states, offering an alternative avenue for visible light absorption. The even distribution of Fe_2O_3 throughout the ZnO matrix in the ZnO : Fe_2O_3 = 3 : 2 sample, augmenting the surface area, may be the cause of its superior photocatalytic performance relative to other specimens. The ZnO : Fe_2O_3 weight ratio of 3 : 2 seems to be the optimum content; a higher Fe_2O_3 content causes a reduction in the separation of photoelectrons from photoholes.

In the aqueous medium, under illumination, the release of Zn^{2+} ions into the solution occurs as ZnO undergoes self-oxidation initiated by the photoexcited valence band holes or photoexcited conduction band electrons in the corrosion process called photocorrosion, which can be represented by the following equations:[87]

$$ZnO + 2h^+ \rightarrow Zn^{2+} + \frac{1}{2}O_2 \quad (5)$$

$$ZnO + 2e^- \rightarrow Zn^{2+} + 2O^- \quad (6)$$

The cooperative interaction of ZnO and Fe_2O_3 enhances the effective capture of photogenerated h^+ and e^- species, thereby mitigating photocorrosion. e^-/h^+ can be trapped in the active sites on the surface of the photocatalyst, electrons reduce surface-adsorbed oxygen to form superoxide ($^{\bullet}O_2^-$), and holes oxidize H_2O to form hydroxyl radicals ($^{\bullet}OH$), which are called reactive oxygen species (ROS). These ROS are reactive species that will degrade MB dye to CO_2, H_2O, and other by-products.[90,97] The population density of ROS in the photocatalytic system depends on the delivery ability of the excited charge carriers to the adsorbed species before recombination. ZnO suffers from the rapid recombination of the photoinduced electrons and holes; *i.e.*, a considerable portion of excitons undergo radiative recombination, diminishing the production of ROS and adversely impacting its photocatalytic efficacy. The establishment of a heterojunction represents a viable strategy to enhance the segregation of photogenerated carriers. Combining ZnO and Fe_2O_3 can achieve a photocatalyst with superior features due to the quantum confinement effect and the charge separation. This intrinsic separation directs electrons and holes in opposing directions, facilitated by the built-in electric field.[75,98] The formation of a heterojunction architecture between these materials led to significantly enhanced efficiency in comparison to bare Fe_2O_3. The notably superior degradation of MB observed with ZnO/Fe_2O_3 unequivocally highlights the enhancing effect of Fe_2O_3 on the production of ROS within the system. The pollutants that adhered to the active sites on the surface of the photocatalyst were mineralized as follows:[98]

$$\text{Photocatalyst} + \text{light} \rightarrow e^- + h^+ \quad (7)$$

$$O_2 + e- \rightarrow {}^{\bullet}O_2^- \quad (8)$$

$$OH^- + h^+ \rightarrow {}^{\bullet}OH \quad (9)$$

$$H_2O + h^+ \rightarrow H^+ + {}^{\bullet}OH \quad (10)$$

$$O_2 + 2H^+ + 2e^- \rightarrow H_2O_2 \quad (11)$$

$$H_2O_2 \rightarrow {}^{\bullet}OH + {}^{\bullet}OH \quad (12)$$

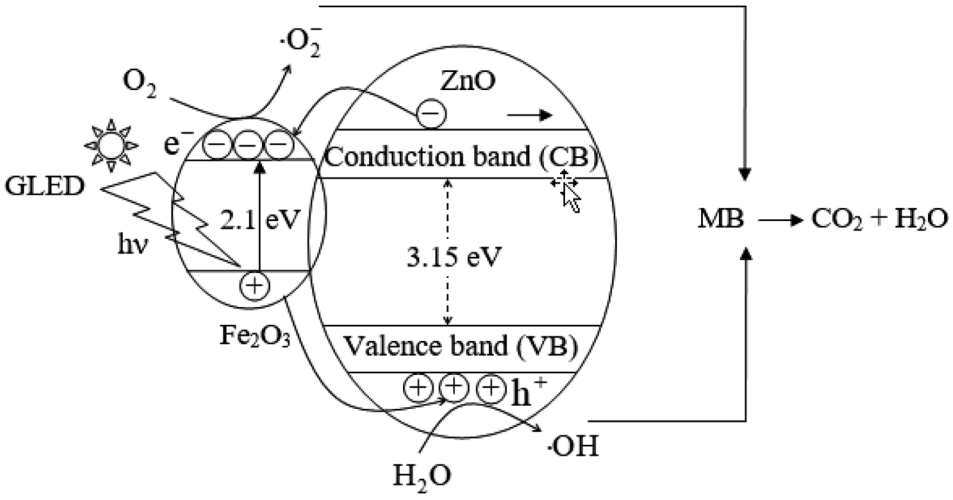

Fig. 12 A schematic diagram showing the role of the heterojunction of ZnO/Fe_2O_3.

$$MB + {}^{\cdot}OH \rightarrow CO_2 + H_2O + \text{by-products} \quad (13)$$

$$MB + {}^{\cdot}O_2^- \rightarrow H_2O + CO_2 + \text{by-products} \quad (14)$$

The by-products, such as NO_2, HCl, SO_2, *etc.*, contain N, Cl, and S. The presence of both O_2 and H_2O hinders the recombination of electrons and holes. Dissolved oxygen and water are essential for initiating reactive radical formation in the photocatalytic process. The interaction between h^+ and OH^- could result in the generation of $^{\cdot}OH$ (eqn (9)), so $^{\cdot}OH$ is the predominant oxidation species in the alkaline medium. The holes generated through light exposure can also engage in the oxidation of water, yielding $^{\cdot}OH$ (eqn (10)). Hydrogen peroxide (H_2O_2) can be formed from O_2, H^+, and e^- (eqn (11)) and then decompose to $^{\cdot}OH$ (eqn (12)), thus promoting the degradation process. ZnO is corroded in an acidic aqueous solution, therefore, its effectiveness is limited in acidic conditions. Conversely, in alkaline media, the surface ZnO acquires a negative charge through the adsorption of hydroxyl ions, facilitating the production of additional $^{\cdot}OH$ species,[99] so ZnO is more favorable in an alkaline medium. Fig. 12 depicts the formation of reactive species in photocatalysts under the excitation of light photons. $^{\cdot}OH$ species exhibit potent oxidizing properties because they have a strong attraction to electrons, whereas $^{\cdot}O_2^-$ can either release electrons or attract holes, thereby acquiring strong reducing capabilities. The pollutants will undergo a reduction reaction by superoxide species in the conduction band and an oxidation reaction by hydroxyl radicals in the valence band. Nonetheless, $^{\cdot}O_2^-$ exerts minimal influence on the photodegradation of MB, while the involvement of $^{\cdot}OH$ in the photocatalytic activity of MB over ZnO/Fe_2O_3 nanocomposite is evident. This result corresponds with a prior study that examined the degradation of MB employing ZnO/CuO nanocomposite.[100]

The adsorption of pollutants on the active sites of the photocatalyst surface due to coulombic attraction depends on the nature of the pollutants and catalyst. The photoexcitation of electrons and holes occurs at the surface and initiates a redox reaction at the liquid–catalyst interface. Pollutants adsorbed on or near the surface of the catalysts will be degraded faster. CO_2 and H_2O are the end products of pollutant degradation in an efficient photocatalytic process, thereby preventing the formation of secondary pollutants. The superior photocatalytic efficacy exhibited by the ZnO/Fe_2O_3 nanocomposites fabricated in this study can be attributed to their high specific surface area.

The heterostructure between ZnO and Fe_2O_3 is the most important factor for enhancing the photocatalytic activity of ZnO/Fe_2O_3. Additionally, the introduction of Fe_2O_3 nanospindles increases the surface area for the adsorption of MB molecules and average porous pore size formed from the adjacent ZnO nanoplates, which is favorable for photocatalytic performance. These less dense materials could facilitate the transport of reactants and products through the photocatalysts.

4. Conclusion

The hydrothermal method has been successfully used to prepare ZnO nanoplates and Fe_2O_3 nanospindles. Mechanical mixing was used to form a heterojunction between the Fe_2O_3 nanospindles and the ZnO nanoplates. Various analytical techniques were used to characterize the as-synthesized samples. The average thickness and width of ZnO nanorods were 20 nm and 100 × 200 nm, and the average length and diameter of Fe_2O_3 nanospindles were 500 nm and 50 nm, respectively. The photocatalytic degradation of methylene blue under GLED light was subsequently analyzed. The ZnO/Fe_2O_3 composite showed a remarkably enhanced photocatalytic performance compared to pristine ZnO nanoplates and Fe_2O_3 nanospindles. The decreased rate of electron–hole recombination was attributed to the suitable contact between ZnO and Fe_2O_3. The weight ratio of ZnO : Fe_2O_3 = 3 : 2, with the highest photocatalytic efficiency of 99.3% after 85 min of GLED illumination. The optimal photocatalytic performance was recorded when the photocatalyst dosage was 0.25 g l^{-1} and decreased at a higher dosage. The role of surface area, heterostructure,

electron–hole separation, and the synergistic effect between Fe_2O_3 and ZnO are the possible reasons for the enhanced photocatalytic activity under visible light compared with pure ZnO or Fe_2O_3. A schematic energy band diagram was suggested to elucidate the formation of a heterojunction between Fe_2O_3 nanospindles and ZnO nanoplates. The limitation of ZnO was resolved by creating heterojunctions and modifying the surface area, which led to impressive charge separation efficiency. Fe_2O_3 has demonstrated a protective role against the photocorrosion of ZnO and facilitated photocatalytic activity. The straightforward fabrication process and promising photocatalytic performance of the ZnO/Fe_2O_3 composite suggest its potential applications for the treatment of textile effluents using visible light.

Author contributions

Nguyen Dac Dien: writing original draft, visualization, validation; Thi Thu Ha Pham, Pham Thi Nga: conceptualization, methodology, data curation; Xuan Hoa Vu, Tran Thi Kim Chi: writing original draft, supervision, reviewing and editing; Nguyen Van Hao, Tran Thi Huong Giang, Nguyen Duc Toan: data curation, resources; Tran Thu Trang, Thi Thu Thuy Nguyen, Vuong Truong Xuan: data curation, reviewing and editing.

Conflicts of interest

The authors declare that they have no competing financial interests in this paper.

Acknowledgements

The authors would like to acknowledge the support of partially funded by the TNU-University of Sciences under the project code: CS2024-TN06-12 and project of Vietnam Trade Union University under grant number: 1697/QD-DHCD in 2023.

References

1 P. Ghasemipour, M. Fattahi, B. Rasekh and F. Yazdian, *Sci. Rep.*, 2020, **10**(1), 4414.
2 I. Khan, K. Saeed, I. Zekker, B. Zhang, A. H. Hendi, A. Ahmad, S. Ahmad, N. Zada, H. Ahmad, L. A. Shah, T. Shah and I. Khan, *Water*, 2022, **14**, 242.
3 S. O. Fatin, H. N. Lim, W. T. Tan and N. M. Huang, *Int. J. Electrochem. Sci.*, 2012, **7**, 9074–9084.
4 S. Nachimuthu, S. Thangavel, K. Kannan, V. Selvakumar, K. Muthusamy, M. R. Siddiqui, S. M. Wabaidur and C. Parvathiraja, *Chem. Phys. Lett.*, 2022, **804**, 139907.
5 P. Pichat, *Photocatalysis and Water Purification: from Fundamentals to Recent Applications,* Wiley-VCH Verlag, 2013.
6 N. Morales-Flores, U. Pal and E. S. Mora, *Appl. Catal., A*, 2011, **394**(1–2), 269–275.
7 E. Brillas, *Chemosphere*, 2020, **250**, 126198.
8 K. G. Pavithra, P. S. Kumar, V. Jaikumar and P. S. Rajan, *J. Ind. Eng. Chem.*, 2019, **75**, 1–19.
9 S. Balu, S. Velmurugan, S. Palanisamy, S.-W. Chen, V. Velusamy, T. C. K. Yang and E.-S. I. El-Shafey, *J. Taiwan Inst. Chem. Eng.*, 2019, **99**, 258–267.
10 M. A. Henderson, *Surf. Sci. Rep.*, 2011, **66**(6–7), 185–297.
11 S. Sato, *Chem. Phys. Lett.*, 1986, **123**(1–2), 126–128.
12 T. L. Villarreal, R. Gómez, M. González and P. Salvador, *J. Phys. Chem. B*, 2004, **108**(52), 20278–20290.
13 L. Song, S. Zhang, B. Chen, J. Ge and X. Jia, *Colloids Surf., A*, 2010, **360**, 1–5.
14 A. A. Yaqoob, N. H. b. M. Noor, A. Serrà and M. N. M. Ibrahim, *Nanomaterials*, 2020, **10**, 932.
15 N. Shimosako and H. Sakama, *Thin Solid Films*, 2021, **732**, 138786.
16 K. Shanthini, V. Manivannan, K. M. Govindaraju, V. C. A. Prakash, G. S. Lekshmi and R. Govindan, *J. Mater. Sci.: Mater. Electron.*, 2022, **33**(19), 15393–15407.
17 N. D. Dien, P. T. T. Ha, X. H. Vu, T. T. Trang, T. D. T. Giang and N. T. Dung, *RSC Adv.*, 2023, **13**(35), 24505–24518.
18 U. T. D. Thuy, I. Borisova, O. Stoilova, I. Rashkov and N. Q. Liem, *Catal. Lett.*, 2018, **148**, 2756–2764.
19 H. Yamashita, Y. Ichihashi, M. Takeuchi, S. Kishiguchi and M. Anpo, *J. Synchrotron Radiat.*, 1999, **6**(3), 451–452.
20 U. Alam, A. Khan, D. Ali, D. Bahnemann and M. Muneer, *RSC Adv.*, 2018, **8**, 17582–17594.
21 H. N. T. Phung, N. D. Truong, L. T. Nguyen, K. L. P. Thi, P. A. Duong and V. T. H. Le, *J. Nonlinear Opt. Phys. Mater.*, 2015, **24**(4), 1550052.
22 N. M. Shooshtari and M. M. Ghazi, *Chem. Eng. J.*, 2017, **315**, 527–536.
23 F. Achouri, S. Corbel, A. Aboulaich, L. Balan, A. Ghrabi, M. B. Said and R. Schneider, *J. Phys. Chem. Solids*, 2014, **75**(10), 1081–1087.
24 Y. Li, J. Wang, B. Liu, L. Dang, H. Yao and Z. Li, *Chem. Phys. Lett.*, 2011, **508**(1–3), 102–106.
25 J. Xiao, J. Lv and Q. Lu, *Mater. Lett.*, 2022, **311**, 131580.
26 V. A. Coleman and C. Jagadish, *Basic Properties and Applications of ZnO, Zinc Oxide Bulk, Thin Films and Nanostructures,* Elsevier Limited, 2006.
27 M. L. Maya-Treviño, M. Villanueva-Rodríguez, J. L. Guzmán-Mar, L. Hinojosa-Reyes and A. Hernández-Ramírez, *Photochem. Photobiol. Sci.*, 2015, **14**, 543–549.
28 J. Gupta, K. C. Barick and D. Bahadur, *J. Alloys Compd.*, 2011, **509**(23), 6725–6730.
29 J. Xie, L. Zhang, M. Li, Y. Hao, Y. Lian, Z. Li and Y. Wei, *Ceram. Int.*, 2015, **41**(8), 9420–9425.
30 M. Aslam, I. M. I. Ismail, T. Almeelbi, N. Salah, S. Chandrasekaran and A. Hameed, *Chemosphere*, 2014, **117**, 115–123.
31 A. Hameed, M. Aslam, I. M. I. Ismail, S. Chandrasekaran, M. W. Kadi and M. A. Gondal, *Appl. Catal., B*, 2014, **160**, 227–239.
32 U. Alam, A. Khan, W. Raza, A. Khan, D. Bahnemann and M. Muneer, *Catal. Today*, 2017, **284**, 169–178.
33 J. Wang, Y. Xia, H. Zhao, G. Wang, L. Xiang, J. Xu and S. Komarneni, *Appl. Catal., B*, 2017, **206**, 406–416.

34 N. Suganthi, S. Thangavel and K. Kannan, *FlatChem*, 2020, **24**, 100197.
35 P. Cheng, Y. Wang, L. Xu, P. Sun, Z. Su, F. Jin, F. Liu, Y. Sun and G. Lu, *Mater. Lett.*, 2016, **175**, 52–55.
36 S. Sakthivel, B. Neppolian, M. V. Shankar, B. Arabindoo, M. Palanichamy and V. Murugesan, *Sol. Energy Mater. Sol. Cells*, 2003, **77**(1), 65–82.
37 O. E. Cigarroa-Mayorga, *Mater. Today Commun.*, 2022, **33**, 104879.
38 D. K. L. Harijan, S. Gupta, S. K. Ben, A. Srivastava, J. Singh and V. Chandra, *Phys. B*, 2022, **627**, 413567.
39 F. u. Zaman, B. Xie, J. Zhang, T. Gong, K. Cui, L. Hou, J. Xu, Z. Zhai and C. Yuan, *Nanomaterials*, 2021, **11**, 3239.
40 F. S. Hashim, A. F. Alkaim, S. M. Mahdi and A. H. O. Alkhayatt, *Compos. Commun.*, 2019, **16**, 111–116.
41 N. Li, J. Zhang, Y. Tian, J. Zhao, J. Zhang and W. Zuo, *Chem. Eng. J.*, 2017, **308**, 377–385.
42 Y. Liu, L. Sun, J. Wu, T. Fang, R. Cai and A. Wei, *Mater. Sci. Eng. B*, 2015, **194**, 9–13.
43 M. I. Rahmah, R. S. Sabry and W. J. Aziz, *Int. J. Miner., Metall. Mater.*, 2021, **28**(6), 1072–1079.
44 A. Hernandez, L. Maya, E. Sanchez-Mora and E. M. Sanchez, *J. Sol-Gel Sci. Technol.*, 2007, **42**, 71–78.
45 J. Trakulmututa, C. Chuaicham, S. Shenoy, A. Srikhaow, K. Sasaki and S. M. Smith, *Opt. Mater.*, 2022, **133**, 112941.
46 R. Youcef, A. Benhadji, D. Zerrouki, N. Fakhakh, H. Djelal and M. T. Ahmed, *React. Kinet. Mech. Catal.*, 2021, **133**, 541–561.
47 J. Zhang, T. Chen, J. Yu, C. Liu, Z. Yang, H. Lu, F. Yin, J. Gao, Q. Liu and X. Zhang, *J. Mater. Sci.: Mater. Electron.*, 2016, **27**, 10667–10672.
48 Y. Lv, J. Liu, Z. Zhang, W. Zhang, A. Wang, F. Tian, W. Zhao and J. Yan, *Mater. Chem. Phys.*, 2021, **267**, 124703.
49 L. Xu, Y. Zhou, Z. Wu, G. Zheng, J. He and Y. Zhou, *J. Phys. Chem. Solids*, 2017, **106**, 29–36.
50 C. Chen, X. Liu, Q. Fang, X. Chen, T. Liu and M. Zhang, *Vacuum*, 2020, **174**, 109198.
51 M. S. AlSalhi, A. Sakthisabarimoorthi, S. Devanesan, S. A. Martin Britto Dhas and M. Jose, *J. Mater. Sci.: Mater. Electron.*, 2019, **30**, 13708–13718.
52 X. Zou, H. Fan, Y. Tian and S. Yan, *CrystEngComm*, 2014, **16**, 1149–1156.
53 E. Mugunthan, M. B. Saidutta and P. E. Jagadeeshbabu, *J. Photochem. Photobiol., A*, 2019, **383**, 111993.
54 R. Qiu, D. Zhang, Y. Mo, L. Song, E. Brewer, X. Huang and Y. Xiong, *J. Hazard. Mater.*, 2008, **156**(1–3), 80–85.
55 R. D. C. Soltani, A. Rezaee, A. R. Khataee and M. Safari, *J. Ind. Eng. Chem.*, 2014, **20**(4), 1861–1868.
56 C. Zhang, N. Li, D. Chen, Q. Xu, H. Li, J. He and J. Lu, *J. Alloys Compd.*, 2021, **885**, 160987.
57 M. D. L. R. Peralta, U. Pal and R. S. Zeferino, *ACS Appl. Mater. Interfaces*, 2012, **4**, 4807–4816.
58 J.-C. Sin, S.-M. Lam, K.-T. Lee and A. R. Mohamed, *J. Mol. Catal. A: Chem.*, 2015, **409**, 1–10.
59 J.-C. Sin, S.-M. Lam, I. Satoshi, K.-T. Lee and A. R. Mohamed, *Appl. Catal., B*, 2014, **148**, 258–268.
60 T. Bora, P. Sathe, K. Laxman, S. Dobretsov and J. Dutta, *Catal. Today*, 2017, **284**, 11–18.
61 I. J. Ani, U. G. Akpan, M. A. Olutoye and B. H. Hameed, *J. Clean. Prod.*, 2018, **205**, 930–954.
62 S. Le, T. Jiang, Y. Li, Q. Zhao, Y. Li, W. Fang and M. Gong, *Appl. Catal., B*, 2017, **200**, 601–610.
63 M. Nami, S. Sheibani and F. Rashchi, *Mater. Sci. Semicond. Process.*, 2021, **135**, 106083.
64 N. Davari, M. Farhadian, A. R. S. Nazar and M. Homayoonfal, *J. Environ. Chem. Eng.*, 2017, **5**, 5707–5720.
65 M. Harati, A. J. Jafari, M. Farzadkia and R. R. Kalantary, *J. Environ. Health Sci. Eng.*, 2022, **20**, 101–112.
66 G.-Y. Zhang, Y. Feng, Y.-Y. Xu, D.-Z. Gao and Y.-Q. Sun, *Mater. Res. Bull.*, 2012, **47**(3), 625–630.
67 M. Liu, P. Song, Z. Yang and Q. Wang, *Ceram. Int.*, 2021, **47**(9), 12181–12188.
68 L. Li, Y. Chen, X. Liu, Q. Wang, L. Du, X. Chen and G. Tian, *Sol. Energy*, 2021, **220**, 843–851.
69 R. Rajendran, Z. Yaakob, M. A. M. Teridi, M. S. Abd Rahaman and K. Sopian, *Mater. Lett.*, 2014, **133**, 123–126.
70 S. G. Yang, X. Quan, X. Li, Y. Z. Liu, S. Chen and G. Chen, *Phys. Chem. Chem. Phys.*, 2004, **6**(3), 659–664.
71 F. Bagheri and N. Chaibakhsh, *Sep. Sci. Technol.*, 2021, **56**(17), 3022–3032.
72 Y. Shi, H. Li, L. Wang, W. Shen and H. Chen, *ACS Appl. Mater. Interfaces*, 2012, **4**(9), 4800–4806.
73 S. Filipović, N. Obradović, L. Anđelković, D. Olćan, J. S. Petrović, M. M. Mirković, V. B. Pavlović, D. Jeremić, B. Vlahović and A. Đorđević, *Sci. Sinter.*, 2021, **53**(1), 1–8.
74 R. Suresh, C. Sandoval, E. Ramírez, Á. Álvarez, H. D. Mansilla, R. V. Mangalaraja and J. Yáñez, *J. Mater. Sci.: Mater. Electron.*, 2018, **29**, 20347–20355.
75 W. Yan, H. Fan and C. Yang, *Mater. Lett.*, 2011, **65**(11), 1595–1597.
76 M. L. Maya-Treviño, M. Villanueva-Rodríguez, J. L. Guzmán-Mar, L. Hinojosa-Reyes and A. Hernández-Ramírez, *Photochem. Photobiol. Sci.*, 2015, **14**, 543–549.
77 J. Xie, Z. Zhou, Y. Lian, Y. Hao, P. Li and Y. Wei, *Ceram. Int.*, 2015, **41**(2), 2622–2625.
78 P. Kumar, T. Khatri, H. Bawa and J. Kaur, *AIP Conf. Proc.*, 2017, **1860**(1), 020065.
79 Y. Li, G. Wei, L. Shao, Z. Li, F. Yu, J. Liu, X. Yang, Q. Lu, A. Li and Y. Huang, *J. Clean. Prod.*, 2019, **207**, 717–727.
80 P. Semeraro, S. Bettini, S. Sawalha, S. Pal, A. Licciulli, F. Marzo, N. Lovergine, L. Valli and G. Giancane, *Nanomaterials*, 2020, **10**(8), 1458.
81 N. D. Dien, L. H. Phuoc, V. X. Hien, D. D. Vuong and N. D. Chien, *J. Electron. Mater.*, 2017, **46**, 3309–3316.
82 X. H. Vu, L. H. Phuoc, N. D. Dien, T. T. H. Pham and L. D. Thanh, *J. Electron. Mater.*, 2019, **48**(5), 2978–2985.
83 D. K. L. Harijan, S. Gupta, S. K. Ben, A. Srivastava, J. Singh and V. Chandra, *Phys. B*, 2022, **627**, 413567.
84 S. Sakthivel, S. U. Geissen, D. W. Bahnemann, V. Murugesan and A. Vogelpohl, *J. Photochem. Photobiol., A*, 2002, **148**(1–3), 283–293.

85 J. Tauc, *Optical Properties of Amorphous Semiconductors,* Plenum Publishing Company Ltd, 1974.
86 P. Sathishkumar, R. Sweena, J. J. Wu and S. Anandan, *Chem. Eng. J.*, 2011, **171**(1), 136–140.
87 M. T. Qamar, M. Aslam, I. M. I. Ismail, N. Salah and A. Hameed, *Chem. Eng. J.*, 2016, **283**, 656–667.
88 K. Shanthini, V. Manivannan, K. M. Govindaraju, V. C. A. Prakash, G. S. Lekshmi and R. Govindan, *J. Mater. Sci.: Mater. Electron.*, 2022, **33**, 15393–15407.
89 S. U. Islam, U. Latief, I. Ahmad, Z. Khan, J. Ali and M. S. Khan, *J. Mater. Sci.: Mater. Electron.*, 2022, **33**(29), 23137–23152.
90 Y. Liu, L. Sun, J. Wu, T. Fang, R. Cai and A. Wei, *Mater. Sci. Eng. B*, 2015, **194**, 9–13.
91 K. Mageshwari, D. Nataraj, T. Pal, R. Sathyamoorthy and J. Park, *J. Alloys Compd.*, 2015, **625**, 362–370.
92 T. T. Minh, N. T. T. Tu, T. T. Van Thi, L. T. Hoa, H. T. Long, N. H. Phong, T. L. M. Pham and D. Q. Khieu, *J. Nanomater.*, 2019, **2019**, 5198045.
93 I. Udom, P. D. Myers, M. K. Ram, A. F. Hepp, E. Archibong, E. K. Stefanakos and D. Y. Goswami, *Am. J. Anal. Chem.*, 2014, **5**, 743–750.
94 Z. Ghasemi, H. Younesi and A. A. Zinatizadeh, *Chemosphere*, 2016, **159**, 552–564.
95 S. Shekoohiyan, A. Rahmania, M. Chamack, G. Moussavi, O. Rahmanian, V. Alipour and S. Giannakis, *Sep. Purif. Technol.*, 2020, **242**, 116821.
96 W. Zhang, X. Li, Q. Zhao, Y. Hou, Y. Shen and G. Chen, *Mater. Chem. Phys.*, 2011, **129**, 683–687.
97 J. Xie, Z. Zhou, Y. Lian, Y. Hao, P. Li and Y. Wei, *Ceram. Int.*, 2015, **41**, 2622–2625.
98 Q. Yin, R. Qiao, L. Zhu, Z. Li, M. Li and W. Wu, *Mater. Lett.*, 2014, **135**, 135–138.
99 K. M. Lee and S. B. Abd Hamid, *Materials*, 2015, **8**(1), 339–354.
100 W. Kumala, *Mediterr. J. Chem.*, 2020, **10**(7), 659–667.